Supplementary Information for

Interlayer Valley Coupling and Hybridized Excitons in Twisted van der Waals Bilayers with Broken Translational Symmetry

Xing Xie[1,2], Junying Chen[1,2], Shaofei Li[1], Junnan Ding[1,2], Jun He[1], Zongwen Liu[3,4], Jian-Tao Wang[5,6,7], Xuewen Wang[8,9,10*], and Yanping Liu[1,2,11*]

1. *Institute of Quantum Physics, School of Physics, Central South University, 932 South Lushan Road, Changsha, Hunan 410083, People's Republic of China*
2. *State Key Laboratory of Precision Manufacturing for Extreme Service Performance, Central South University, 932 South Lushan Road, Changsha, Hunan 410083, People's Republic of China*
3. *School of Chemical and Biomolecular Engineering, The University of Sydney, Sydney, NSW 2006, Australia*
4. *The University of Sydney Nano Institute, The University of Sydney, Sydney, NSW 2006, Australia*
5. *Beijing National Laboratory for Condensed Matter Physics, Institute of Physics, Chinese Academy of Sciences, Beijing 100190, People's Republic of China*
6. *School of Physical Sciences, University of Chinese Academy of Sciences, Beijing 100049, People's Republic of China*
7. *Songshan Lake Materials Laboratory, Dongguan, Guangdong 523808, People's Republic of China*
8. *Frontiers Science Center for Flexible Electronics (FSCFE) & Institute of Flexible Electronics (IFE), Northwestern Polytechnical University, Xi'an 710072, People's Republic of China*
9. *MIIT Key Laboratory of Flexible Electronics (KLoFE), Northwestern Polytechnical University, Xi'an 710072, People's Republic of China*
10. *Shaanxi Key Laboratory of Flexible Electronics (KLoFE), Northwestern Polytechnical University, Xi'an 710072, People's Republic of China*
11. *Shenzhen Research Institute of Central South University, Shenzhen 518000, People's Republic of China*

* Correspondence and requests for materials should be addressed to email: liuyanping@csu.edu.cn, iamxwwang@nwpu.edu.cn

Table of Contents

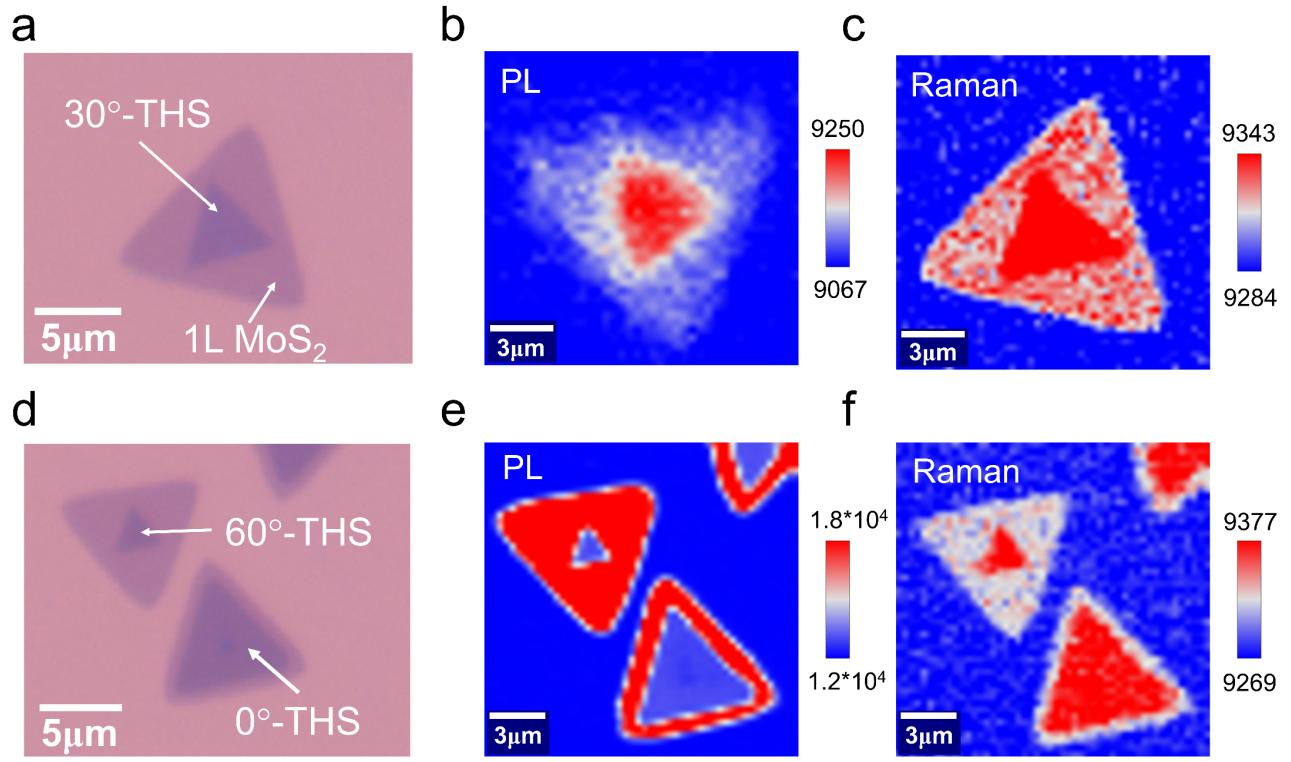

Figure S1. Samples and spectral mapping. a, Optical image of CVD-growth 30° twisted MoS_2 homobilayer (30°-THS). **b-c,** PL (**b**) and Raman (**c**) mapping of 30°-THS with a central energy of 1.936 eV (HIX_A^M) and central wavenumber of 407 cm^{-1} in the broaden of 17 meV and 13 cm^{-1}, respectively. In **b**, the PL intensity of HIX_A^M is uniformly distributed across 30°-THS sample. **d**, Samples of 0° and 60° twisted MoS_2 homobilayers (0°-THS and 60°-THS). **e, f,** PL (**b**) and Raman (**c**) mapping of 0°-THS and 60°-THS with a central energy of 1.825 eV and central wavenumber of 407 cm^{-1} in the broaden of 23 meV and 13 cm^{-1}, respectively.

Supplementary Note 1: Zeeman splitting in hybridized interlayer exciton

The magnetic moments contributing to the Zeeman splitting in K/-K valley of TMDCs mainly include spin, orbital, and valley contributions[1-3]. The total magnetic moment $\mu^{l\xi\kappa s}$ can be written as:

$$\mu^{l\xi\kappa s} = \mu^{ls}_{Spin} + \mu^{l\xi\kappa}_{Orbital} + \mu^{l\xi\kappa}_{Valley} \quad (1)$$

where $l = 1, 2$, $\xi = v, c$ (valence band v and conduction band c), $\kappa = k, -k$, and $s = \uparrow, \downarrow$ present the layer, band, valley, and spin indexes, respectively. The spin magnetic moment is given by

$\mu_{Spin}^{ls} = g_s s_z \mu_B$, with $g_s \approx 2$ for electron factor[4] and $s_z = +\frac{1}{2}, -\frac{1}{2}$ for $\uparrow, \downarrow$, thus $\mu_{Spin}^{ls} \approx \pm\mu_B$. For excitons involving spin-single transition, the Zeeman splitting caused by spin magnetic moment have same shifts for valence and conduction bands and these shifts cancel out under a magnetic field.[2,5] Therefore, the spin magnetic moment does not contribute to the effective Zeeman effect for exciton in same spin transition. It notes that spin-triplet transitions, such as dark exciton[6,7] and triplet interlayer exciton[2,5], are influenced by the spin Zeeman effect, leading to larger Zeeman shifts.

For the orbital magnetic moment, since the conduction bands in K/-K valley are mainly contributed by d_Z^2 orbital,[8] its Zeeman splitting is small and negligible.[1] Consequently, the orbital contribution to the Zeeman effect is dominantly attributed to the valence band. Its magnetic moment is given by $\mu_{Orbital}^{v\kappa} = \pm 2\mu_B$, where ± denotes orbital magnetic moment at –K or K valley. For excitons involving K/-K transitions, the Zeeman shifts contributed by the orbital magnetic moment under magnetic field are $-4\mu_B B$.

Furthermore, due to the interaction between the valley magnetic moment and magnetic field, the valley magnetic moment $\mu_{Valley}^{\xi\kappa} = \kappa\alpha^{\xi}\mu_B$ also contributes to the Zeeman splitting,[1] where $\kappa = \mp 1$ for ±K valley and $\alpha^{\xi} = \frac{m_0}{m_{\xi}^*}$ for the effective mass of valence and conduction bands. We use the calculated effective mass $m_{v1}^* = 0.54m_0$, $m_{v2}^* = 0.61m_0$, $m_{c1}^* = 0.47m_0$, and $m_{c2}^* = 0.44m_0$ ($\xi 1$ and $\xi 2$ represent the first and second valence or conduction bands) for monolayer MoS_2.[9] Therefore, the orbital magnetic moments for the valence and conduction bands are $\mu_{Valley}^{v1} = 1.9\mu_B$, $\mu_{Valley}^{c1} = 2.1\mu_B$, $\mu_{Valley}^{v2} = 1.6\mu_B$, and $\mu_{Valley}^{c2} = 2.3\mu_B$. For intralayer A and B transition, the total orbital magnetic moments in K valley have values of $-0.2\mu_B$ and $-0.7\mu_B$, respectively. Nevertheless, the orbital magnetic moments of $-0.2\mu_B$ ($-0.7\mu_B$) and $4\mu_B$ ($3.9\mu_B$) are found in the R-type and H-type

stacked MoS_2 bilayer for interlayer A (B) transition, respectively.

Summarizing these three magnetic moments contribution, the theoretical estimated Zeeman splitting is given by:

$$\begin{aligned}
\Delta E_A &= E_K - E_{-K} = -2\mu_{Spin}^{A}B - 2\mu_{Orbital}^{A}B - 2\mu_{Valley}^{A}B = -3.6\mu_B B \\
\Delta E_B &= E_K - E_{-K} = -2\mu_{Spin}^{B}B - 2\mu_{Orbital}^{B}B - 2\mu_{Valley}^{B}B = -2.6\mu_B B \\
\Delta E_{IXA} &= E_K - E_{-K} = -2\mu_{Spin}^{IXA}B - 2\mu_{Orbital}^{IXA}B - 2\mu_{Valley}^{IXA}B = -12\mu_B B \\
\Delta E_{IXB} &= E_K - E_{-K} = -2\mu_{Spin}^{IXB}B - 2\mu_{Orbital}^{IXB}B - 2\mu_{Valley}^{IXB}B = -11.8\mu_B B
\end{aligned} \tag{2}$$

Here, the interlayer exciton of H-type MoS_2 are considered. The calculated g factors for A exciton are in agreement with the experimental results of ~-4[10,11] or ~-3[12], but deviate the experimental results of ~-2[3,13] in monolayer or bilayer MoS_2. These different experimental results potentially arise from differences in the samples, many-body interactions or non-single exciton contributions,[3,13] which implies the sensitivity of the g-factor to the band structure. In our measurements, the g factors scatter from -2.4 to -11.5, which shows twisted-angle dependence, with values of -6.9 for 0°-THS, -11.5 for 30°-THS, and -2.4 for 60°-THS (Figure S2). The precise relationship between the g-factor and the twisted angle is not yet understood, and there are no systematic studies directly addressing this, suggesting the need for further investigation. One potential origin is the change in the band structure due to the twisted angle in homobilayer. for example, in H-type MoS_2, the valence bands for different layers are degenerate, whereas in R-type MoS_2, the bands are non-degenerate.[14]

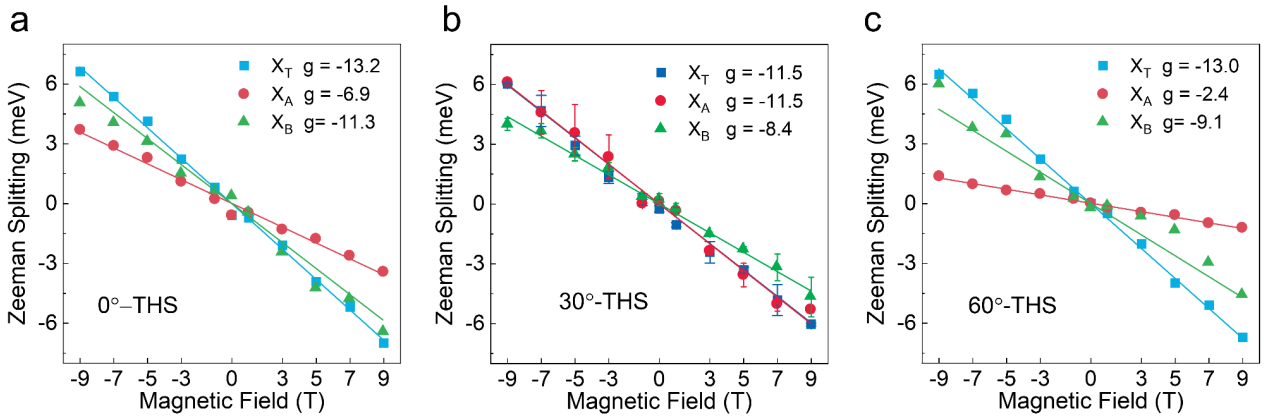

Figure S2. Zeeman splitting in twisted MoS_2 homobilayer. a-c Zeeman splitting as a function of magnetic field for 0°-THS (**a**), 30°-THS (**b**), and 60°-THS (**c**), showing different g-factors. Points are the experimental measured values, while solid lines represent the fitting results using $\Delta E = g\mu_B B$.

Unlike the intralayer exciton in moiré quasicrystal, the coupled interlayer A exciton has a minor Zeeman effect with a splitting of ~0.4 meV under 9 T magnetic field. To understand this abnormal Zeeman effect, we employ the phenomenological model developed by Lorchat et. al..[3] Considering the simplified model, the Bloch equations for only A exciton P^B and interlayer exciton P^{IX} is:

$$\left(\hbar\omega - \varepsilon^A\right)P^A = \Lambda + \eta P^{IX} \tag{3}$$

$$\left(\hbar\omega - \varepsilon^{IX}\right)P^{IX} = \eta P^A \tag{4}$$

where $\varepsilon^A = E^A + g_A B_z$ and $\varepsilon^{IX} = E^{IX} + g_{IX} B_z$ represent the energy at a field and η is the coupling strength between intralayer and interlayer exciton. Moreover, between A and IX, there are an energy difference Ω (detuning energy), i.e. $E^{IX} = E^A + \Omega$. Upon the A coupled IX, the energies have the formation:

$$\left(\hbar\omega\right)_{\pm} = \frac{\varepsilon^A + \varepsilon^{IX}}{2} \pm \sqrt{\frac{\left(\varepsilon^A - \varepsilon^{IX}\right)^2}{4} + \eta^2} = E_A + \frac{\Omega}{2} + \frac{g_A + g_{IX}}{2} B_z \pm \sqrt{\frac{\left(\left(g_A - g_{IX}\right)B_z - \Omega\right)^2}{4} + \eta^2} \tag{5}$$

Here, ± denote the detuning A transition and IX transition, respectively. Therefore, the effective g factor is:

$$g_{\pm}^{eff} = \partial_{B_z}(\hbar\omega)_{\pm}|_{B_z=0} = \frac{(g_A + g_{IX})}{2} \mp \frac{(g_A - g_{IX})\Omega}{4\sqrt{\eta^2 + \frac{\Omega^2}{4}}} \quad (6)$$

This equation suggests that the effective g^{eff} factor of HIX_A^M is correlated to the coupling strength η and detuning Ω. The Ω can be controlled by the electronic field, leading to variation of g^{eff} assuming the electronic field minor effect on η. In 2H-MoS_2 and 2H-$MoSe_2$ bilayer, the g-factor can be tuned from 4.2 to 7[3] and from -1.9 to 11.8[15] under an electronic field, respectively.

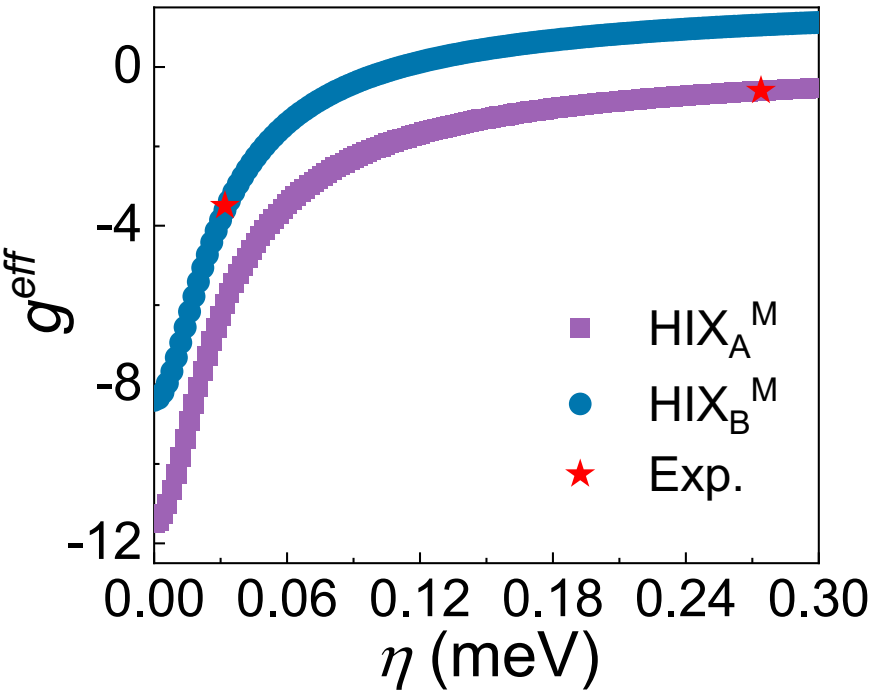

Figure S3. Effective g factor in hybridized interlayer exciton. Effective g factor (g^{eff}) as a function of coupling strength η with the parameters of $g_A = -11.5$, $g_B = -8.4$, $g_{IX} = 12$, and $\Omega = -0.04\text{eV}$. Blue and purple points represent the g^{eff} of HIX_A^M and HIX_B^M, respectively. Red stars represent our experimental measured g factor of HIX_A^M and HIX_B^M, which locate at η of 0.0274 and 0.032 meV.

To obtain the η between intralayer and interlayer excitons, we set a fixed value to Ω due to

absent of the electronic field. Here, the experimental measured g_A (-11.5) and g_B (-8.4), theoretical estimated g_{IX} (12), and $\Omega = -0.04\text{eV}$ [3]are used. Figure S3 shows the calculated g^{eff} with varying coupling strength η. It exhibits pure g factor of A and B excitons in the absent of the coupling of intralayer and interlayer excitons. Our measured g factors of $\text{HIX}_\text{A}^\text{M}$ (-0.6) and $\text{HIX}_\text{B}^\text{M}$ (-3.5) fall on these curves with $\eta = 0.274$ and $\eta = 0.033\,\text{meV}$, respectively. These results indicate the reduced Zeeman splitting when the exciton forms a hybridized state, which nearly eliminates the Zeeman effect in moiré quasicrystal.

Supplementary Note 2: Magnetic-field-dependent valley polarization of hybridized interlayer exciton

The Hamiltonian of the hybridized interlayer exciton can be expressed as follows, considering the strong coupling between the intervalley electron-hole exchange interaction and valley pseudospin[1]:

$$\text{H}_{\text{HIX}^\text{M}} = \hbar\omega_0 + \frac{\hbar^2 k^2}{2M_0} + V'(k) + \zeta_+ V_{\text{intervalley}}(\boldsymbol{k}) + \zeta_- V^*_{\text{intervalley}}(\boldsymbol{k}) + \zeta_+ V_{\text{interlayer}}(\boldsymbol{k}) + \zeta_- V^*_{\text{interlayer}}(\boldsymbol{k}) \quad (7)$$

where $\hbar\omega_0$ and M_0 are the HIX^Ms energy at k=0 and mass, respectively. $V'(k)$ is the intravalley electron-hole exchange, and k is the distance between K and Γ point in the first Brillouin zone. The intervalley electron-hole exchange $V_{\text{intervalley}}(\boldsymbol{k}) = V(k)e^{-2i\theta}$ with the Pauli matrix ζ, and $\boldsymbol{k} \equiv (k_x, k_y) = (k\cos\theta, k\sin\theta)$ is the center-of-mass wavevector. Since HIX^Ms in moiré quasicrystal have interlayer component, electron-hole exchange interaction involves interlayer exchange $V_{\text{interlayer}}(\boldsymbol{k})$.

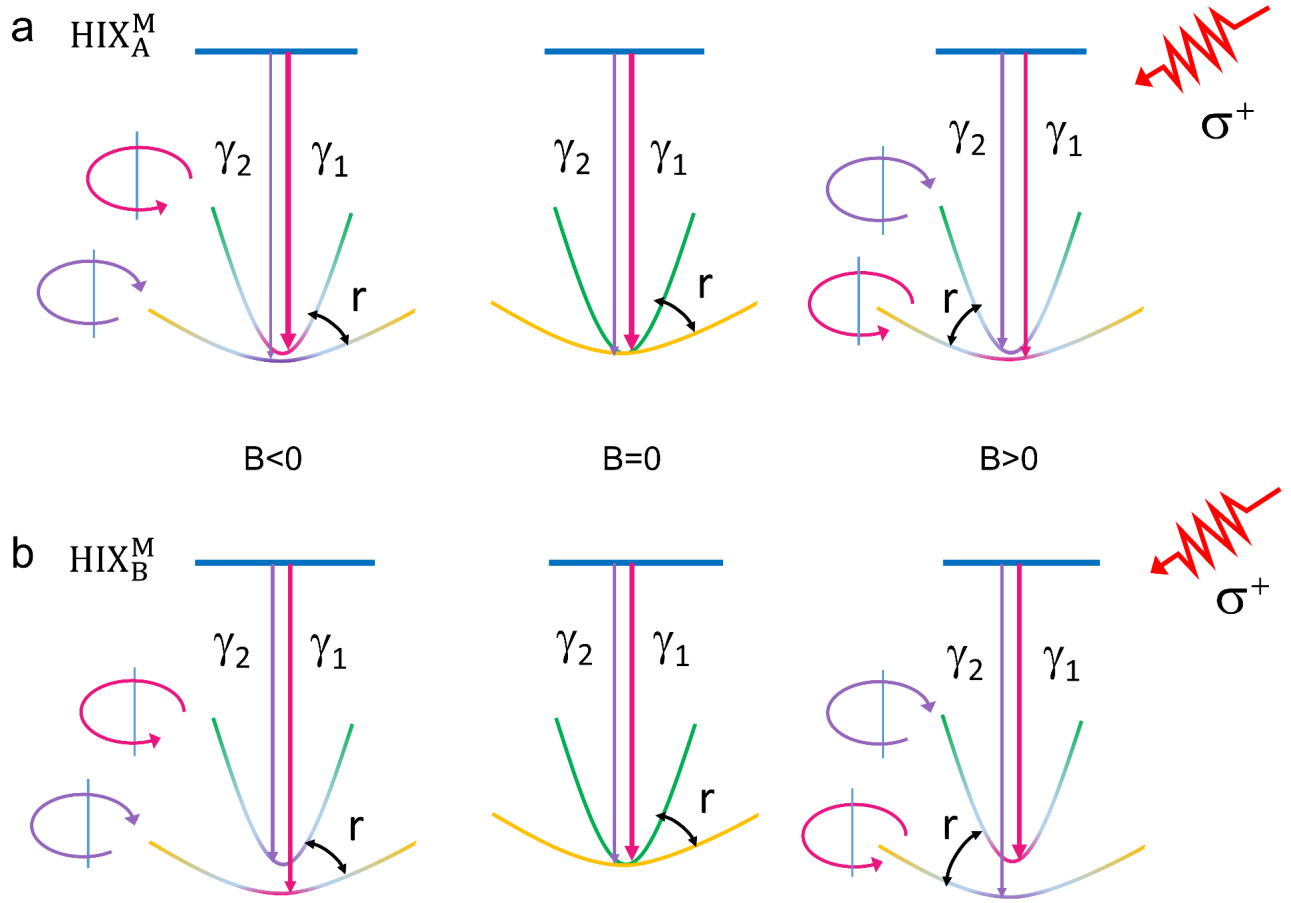

Figure S4. Hybridized exciton energy spectra under magnetic field. a-b, Valley-orbit coupled exciton dispersion spectra of HIX_A^M (**a**) and HIX_B^M (**b**) under B<0 (left panel), B=0 (medium panel), and B>0 (right panel). The purple and pink in exciton dispersion represent the K and –K valley, respectively, while the green and orange denote superposition of K and –K valley. Purple and pink arrows represent valley-flipping and valley-conserving processes during forming the valley exciton with valley-conserving and valley-flipping rate of γ_1 and γ_2, respectively. r is the valley depolarization rate in the exciton ground state before recombination. These schematic diagrams are displayed under σ^+ excitation.

Similar to the neutral A (or B) exciton, the exciton dispersion splits into steeper and flatter branches due to strong electron-hole exchange (Figure S4), corresponding to smaller and larger momenta requirements, respectively.[1] In the absent of field, these two braches touch at the cone, with

the valley-conserving rate γ_1 and valley-flipping rate γ_2 during exciton formation and the valley depolarization rate r in the exciton ground state. For the neutral exciton, the valley-flipping process during exciton formation dominants the valley depolarization. When a magnetic field is applied, the degenerates are lifted due to Zeeman effect with the contrary occupancy to lower and upper branches for the K and -K valley exciton in the B>0 and B<0, leading to the larger (smaller) γ_2/γ_1 at B<0 (B>0) than at the absent of field under σ^+ excitation and the "X" shape magnetic-field-dependent valley polarization for neutral exciton (details see Ref.1). However, due to the inclusion of interlayer intervalley contributions, the exciton dispersions of HIX^Ms are not only affected by the single factor (intralayer and interlayer contribution), resulting in the different case.

For HIX^Ms, the valley-conserving and valley-flipping rate can be descripted by corresponding rates of the intralayer neutral exciton and interlayer hybridized degree, that is, $\gamma_1^{\mathrm{HIX_A^M}} = \alpha_{\mathrm{A}}\gamma_1^{\mathrm{A}}\chi_1^{\mathrm{A}}$ ($\gamma_1^{\mathrm{HIX_B^M}} = \alpha_{\mathrm{B}}\gamma_1^{\mathrm{B}}\chi_1^{\mathrm{B}}$) and $\gamma_2^{\mathrm{HIX_A^M}} = \beta_{\mathrm{A}}\gamma_2^{\mathrm{A}}\chi_2^{\mathrm{A}}$ ($\gamma_2^{\mathrm{HIX_B^M}} = \beta_{\mathrm{B}}\gamma_2^{\mathrm{B}}\chi_2^{\mathrm{B}}$), where γ_1^i and γ_2^i represent valley-conserving and valley-flipping rates for corresponding excitons, respectively. α, β, and χ are the valley-conserving and valley-flipping coefficient and hybridized degree, respectively. For $\mathrm{HIX_A^M}$, magnetic field leads to the increase in γ_1^{A} and χ_1^{A} (due to approaching valley band), while a decrease of γ_2^{A} and χ_2^{A}, under B<0 and σ^+ excitation. These are interchanged under B>0. Therefore, it has $\frac{\gamma_1^{\mathrm{HIX_A^M}}(\mathrm{B<0},\sigma^-)}{\gamma_2^{\mathrm{HIX_A^M}}(\mathrm{B<0},\sigma^-)} > \frac{\gamma_1^{\mathrm{HIX_A^M}}(\mathrm{B=0},\sigma^-)}{\gamma_2^{\mathrm{HIX_A^M}}(\mathrm{B=0},\sigma^-)} > \frac{\gamma_1^{\mathrm{HIX_A^M}}(\mathrm{B>0},\sigma^-)}{\gamma_2^{\mathrm{HIX_A^M}}(\mathrm{B>0},\sigma^-)}$, i.e. $\frac{\alpha_{\mathrm{A}}\gamma_1^{\mathrm{A}}\chi_1^{\mathrm{A}}(\mathrm{B<0},\sigma^-)}{\beta_{\mathrm{A}}\gamma_2^{\mathrm{A}}\chi_2^{\mathrm{A}}(\mathrm{B<0},\sigma^-)} > \frac{\alpha_{\mathrm{A}}\gamma_1^{\mathrm{A}}\chi_1^{\mathrm{A}}(\mathrm{B=0},\sigma^-)}{\beta_{\mathrm{A}}\gamma_2^{\mathrm{A}}\chi_2^{\mathrm{A}}(\mathrm{B=0},\sigma^-)} > \frac{\alpha_{\mathrm{A}}\gamma_1^{\mathrm{A}}\chi_1^{\mathrm{A}}(\mathrm{B>0},\sigma^-)}{\beta_{\mathrm{A}}\gamma_2^{\mathrm{A}}\chi_2^{\mathrm{A}}(\mathrm{B>0},\sigma^-)}$, resulting in the "X" shape. However, for $\mathrm{HIX_B^M}$, they have smaller conserving-flipping ratio $\frac{\gamma_1^{\mathrm{B}}}{\gamma_2^{\mathrm{B}}}$ under B<0 than that at B=0 due to adverse spin relative to A transitions. But $\frac{\chi_1^{\mathrm{B}}}{\chi_2^{\mathrm{B}}}$ still increases under B<0 than that at B=0, since the valley

Zeeman effects do not change the sign for different spin-state excitons (from same valley). When B>0, the $\frac{\gamma_1^{\mathrm{B}}}{\gamma_2^{\mathrm{B}}}$ increases and $\frac{\chi_1^{\mathrm{B}}}{\chi_2^{\mathrm{B}}}$ decreases. These lead to moderate magnetic field effect for $\mathrm{HIX_B^M}$.

Tables S1. Commensurate angles calculated by $\cos(\theta_i)=\frac{\left(3i^2+3i+0.5\right)}{\left(3i^2+3i+1\right)}$ with integer *i* and twisted angle θ_i.

i	1	2	3	4	5	6	7	8	9	10
θ_i (°)	21.8	13.2	9.4	7.3	6.0	5.1	4.4	3.9	3.5	3.2
i	11	12	13	14	15	16	17	18	19	20
θ_i (°)	2.9	2.6	2.5	2.3	2.1	2.0	1.9	1.8	1.7	1.6

Supplementary Note 3: Interlayer hybridized excitons in natural 2L MoS_2

For natural MoS_2 bilayers, the interlayer hybridized excitons (HIX) have been observed[3,14,16-19] due to allowable hole interlayer tunneling.[8,20] These HIXs are formed by interlayer A exciton hybridizing the B exciton, resulting in an anticrossing between HIX and B excitons and splitting of B exciton under an electric field.[17] Moreover, due to hybridization with the B exciton, the sign of g-factor for HIX is opposite to the intralayer excitons.[3] The g-factor of HIX is reduced to around 4, as result of the hybridization effects, and it can be enhanced to 7 when an electric field is applied to detune the B exciton. These hybridization effects are not observed in R-stacked MoS_2 bilayers, which lack interlayer tunneling due to prohibitive symmetry. The commensurate twist angle (Table S1) do

not brighten the direct interlayer exciton, since the restricted conditions are not broken. However, the broken translational symmetry provides the possibility[21-23] by Umklapp process creating the interlayer K and –K coupling, which brightens the interlayer excitons by hybridizing the intralayer excitons. Our measured optical spectra of 11°-THS, 13.2°-THS, and 21.8°-THS (Figure 3 in main text) confirm this point.

Furthermore, we calculated the band structures of THS at twist angle of 0°, 60°, 13.2°, and 21.8° to understand the electronic structures of MoS_2 at different twist angle (Figure S5). We noted that the band structures for 11°-THS and 30°-THS were not calculated due to the lack of periodic lattices. For 0°-THS, the band structure shows a splitting of the valence band at K point, which is not observed in 60°-THS. This splitting arises from the broken degenerate between top and bottom layers,[14] with energy differences of 36 meV and 33 meV for the first and second valence bands, respectively. For 13.2°-THS and 21.8°-THS, the bands from both the top and bottom layers are folded into moiré Brillouin zone (mBZ), creating the folded bands. The flat band effects are significantly weakened relative to that in small twist-angle homobilayers, with bandwidth of 238 meV and 480 meV for first valence band, respectively.

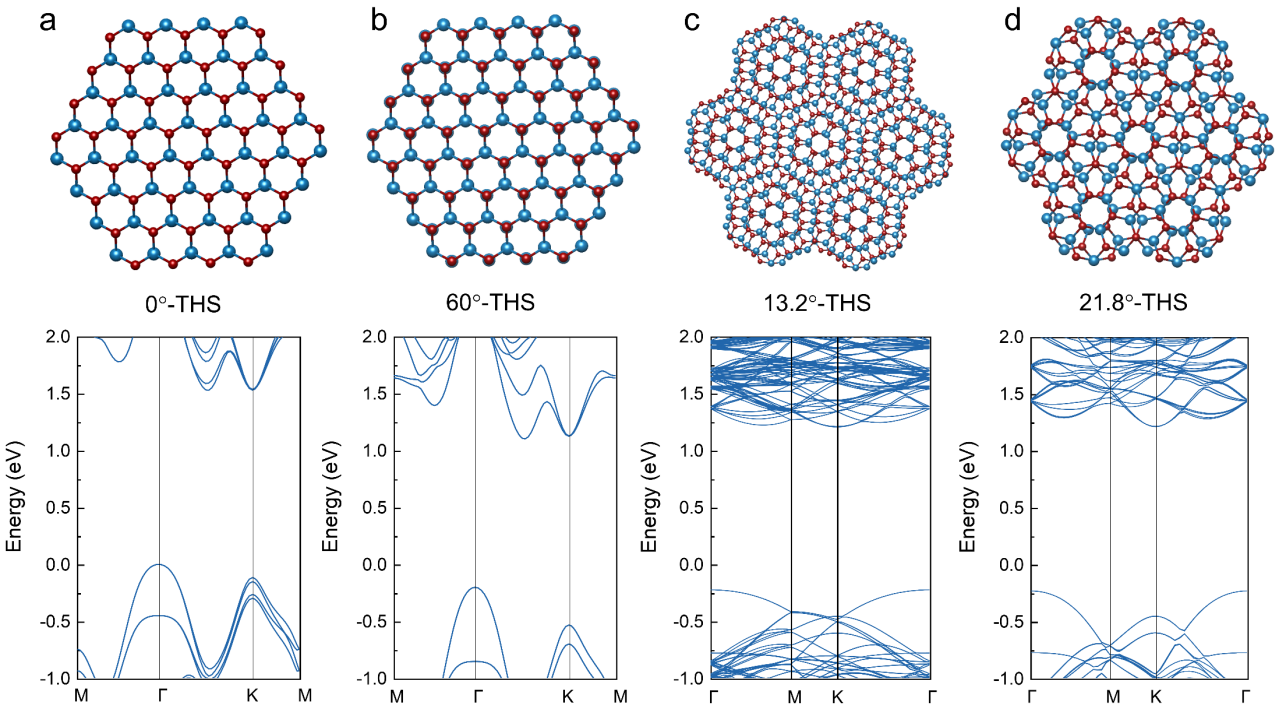

Figure S5. Density functional theory (DFT) calculated band structures. a-d, Structural diagrams (top panels) and band structures (bottom panels) of twisted MoS_2 bilayers at twist angle of 0° (**a**), 60° (**b**), 13.2° (**c**), and 21.8° (**d**). The calculated band structures include the spin-orbit coupling (SOC). The first and second valence bands of 0°-THS at K point are broken the degenerate, arising an energy difference between top and bottom layers,[14] which is contrary to the degenerate bands in 60°-THS.

Supplementary Note 4: Temperature-dependent PL spectra

We use the O'Donnell and Chen model[24] to fit the PL peak positions with temperature:

$$E_g(T) = E_g(0) - S\langle\hbar\omega\rangle\left[\coth\left(\frac{\langle\hbar\omega\rangle}{2k_BT}\right)-1\right] \quad (8)$$

where $E_g(0)$ and $E_g(T)$ represent the band gaps at temperature 0 K and T, respectively. S and $\langle\hbar\omega\rangle$ are the dimensionless fitting parameter related to the strength of electron-phonon interaction and the average phonon energy, respectively. The cosh term accounts for the phonon density at T temperature with Boltzmann constant k_B. The fitting results using this equation is in agreement with our experimental measured data. The fitting parameters are shown in Table S2.

Figure S6 shows temperature-dependent PL spectra of moiré quasicrystal, revealing a blueshift PL energy, broadening of the full width at half maximum (FWHM), and a reduction in intensity. Remarkably, HIX_A^M and HIX_B^M gradually shift towards the X_A and X_B peaks with increasing the temperature, leading to a faster energy shift with temperature (Figure S6d). The energy difference between HIX_A^M (HIX_B^M) and X_A (X_B) decline gradually from ~70 (~85) to ~50 (~55) meV (Figure S6e). This faster blueshift implies a possible energy detuning to X_A or X_B excitons. We rewrite equation (5) at the absent of magnetic field:

$$E_{HIX^M}(T) = E_{intra}(T) + \frac{\Omega(T)}{2} + \sqrt{\frac{\Omega(T)^2}{4} + \eta(T)^2} + c \tag{9}$$

Here, the coupling strength η and detuning parameter Ω are the function of temperature, and c is the correction constant. We assume that the coupling strength η remains constant with temperature, and thus only $\Omega(T)$ detune the energy of HIX^Ms. Using values of $\eta = 0.274$ (0.032) meV obtained from g factor (**Supplementary Note 1**) and c = 0.1811 (0.0792) eV for HIX_A^M (HIX_B^M), the $\Omega(T)$ can be estimated based on our experimental data, as listed in Table S3. The corresponding energy of HIX^M is shown in Figure 4 of main text. The $\Omega(T)$ decrease with increasing the temperature, indicating the temperature detuning energy of interlayer exciton.

Table S2. Fitting parameters of temperature-dependent PL peak positions in 30°-THS, 0°-THS, 60°-THS, 1L-MoS_2 using equation (8).

		X_T	X_A	HIX_A^M	X_B	HIX_A^M
30°-THS	$E_g(0)$	1.841	1.866	1.938	2.005	2.090
	S	1.969	3.347	2.003	2.739	3.060
	$\langle\hbar\omega\rangle$	0.042	0.062	0.027	0.049	0.034
	$S*\langle\hbar\omega\rangle$	0.082	0.208	0.054	0.133	0.104
0°-THS	$E_g(0)$	1.857	1.892		2.020	
	S	1.425	1.526		2.157	
	$\langle\hbar\omega\rangle$	0.020	0.017		0.034	
60-THS	$E_g(0)$	1.855	1.888		2.039	
	S	2.226	2.180		2.020	
	$\langle\hbar\omega\rangle$	0.032	0.028		0.029	
1L-MoS_2	$E_g(0)$	1.853	1.889		2.023	
	S	1.852	2.009		2.754	
	$\langle\hbar\omega\rangle$	0.031	0.025		0.055	

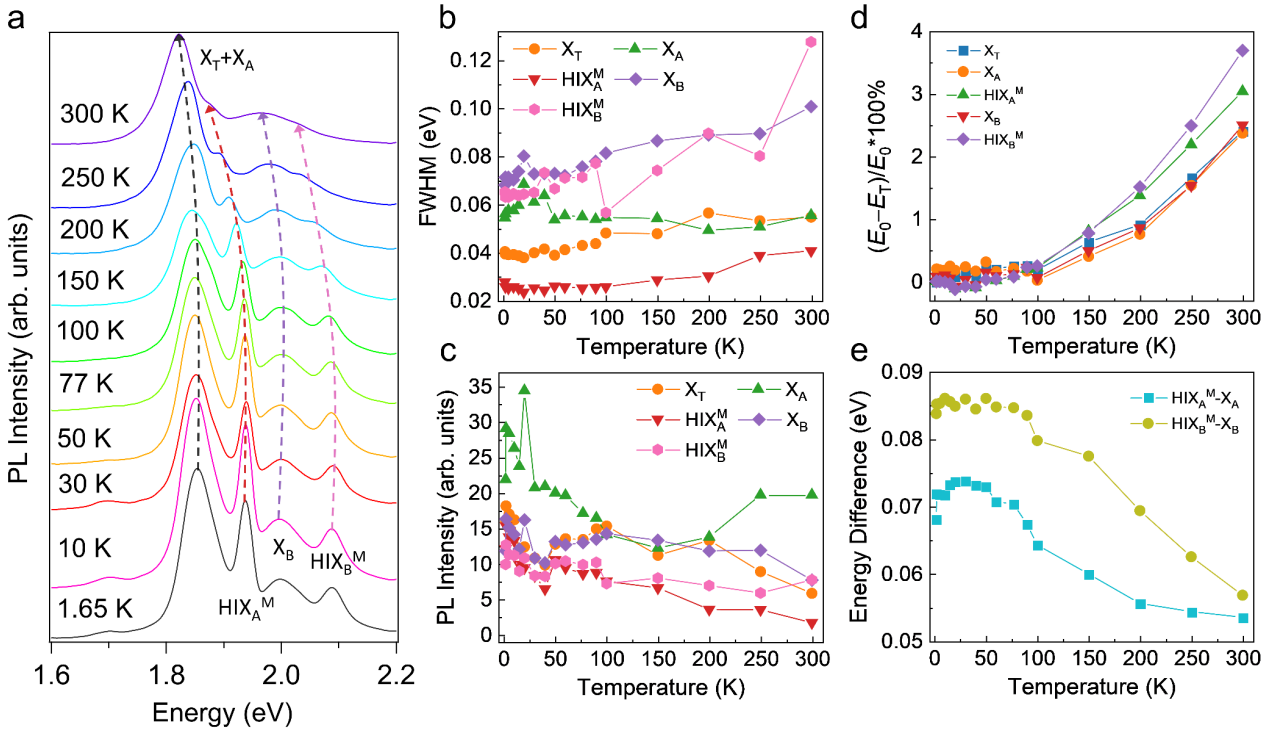

Figure S6. Temperature-dependent PL spectra of 30°-THS. a, PL spectra of 30°-THS at selected temperature. The dotted lines show the trend of PL peaks with increasing the temperature. **b-c**, Peak full width at half maximum (FWHM; **b**) and intensity (**c**) as a function of temperature. **d**, Energy change with temperature. Hybridized excitons have a faster energy shift under high temperature (beyond 100 K) than intralayer excitons that shows near consistent energy shift. **e**, Energy difference between HIX_A^M (HIX_B^M) and X_A (X^B), revealing a reduced energy distance with increasing the temperature.

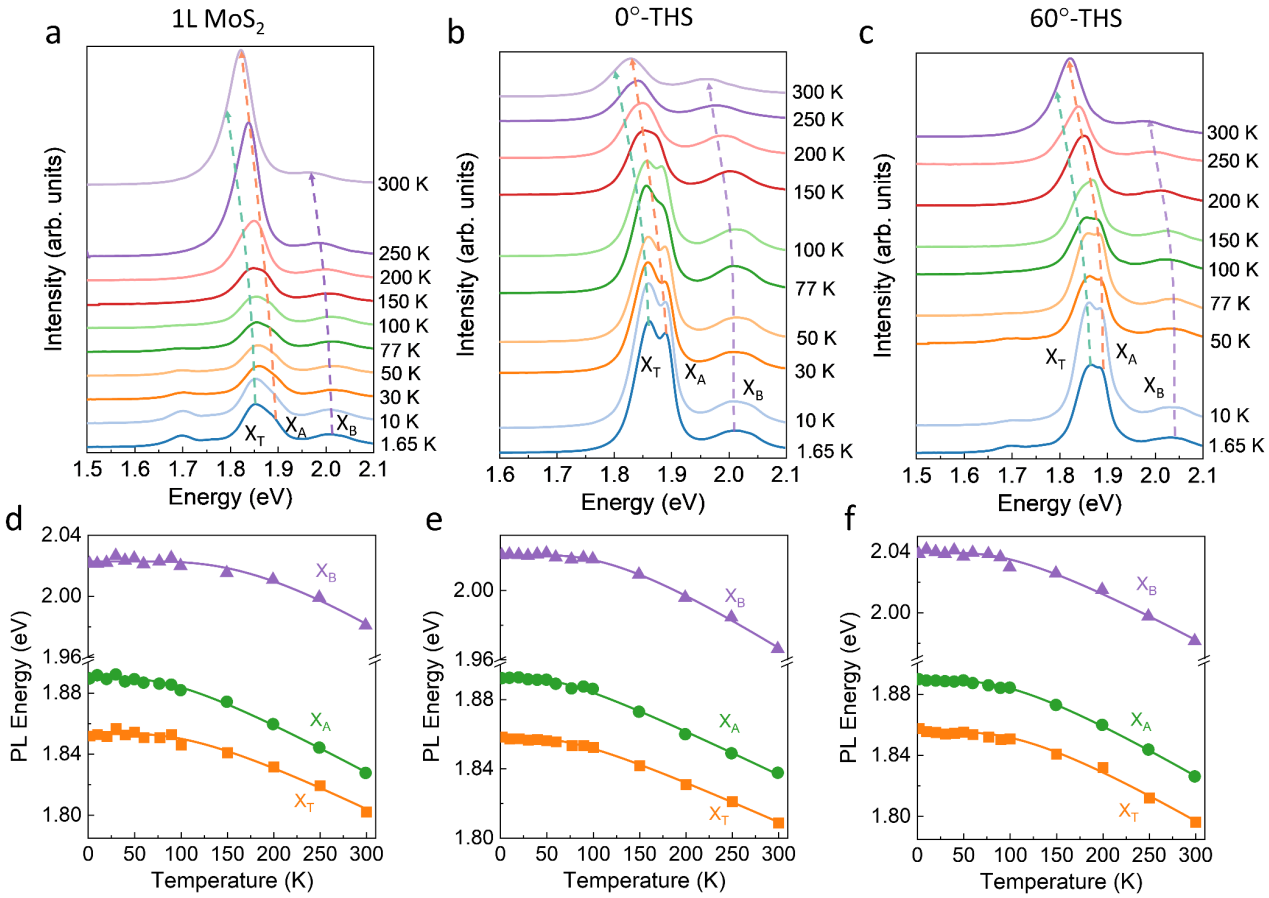

Figure S7. Temperature-dependent PL spectra of 1L MoS_2, 0°-THS, and 60°-THS. a-c, PL spectra of 1L MoS_2 (**a**), 0°-THS (**b**), and 60°-THS (**c**) at selected temperature. The dotted lines represent the temperature-dependent peak shift. **d-f**, PL peaks energy for 1L MoS_2 (**d**), 0°-THS (**e**), and 60°-THS (**f**) as a function of temperature, showing a red shift with increasing the temperature. The points are experimental measured data, while the solid lines denote fitting results through equation (8).

Table S3. Detuning parameters Ω (eV) under different temperature according to equation (9) and experimental data.

T (K)		1.65-90	100	150	200	250	300
HIX_A^M	Ω (eV)	-0.04	-0.052	-0.062	-0.07	-0.072	-0.074
HIX_B^M		-0.04	-0.042	-0.048	-0.055	-0.06	-0.0635

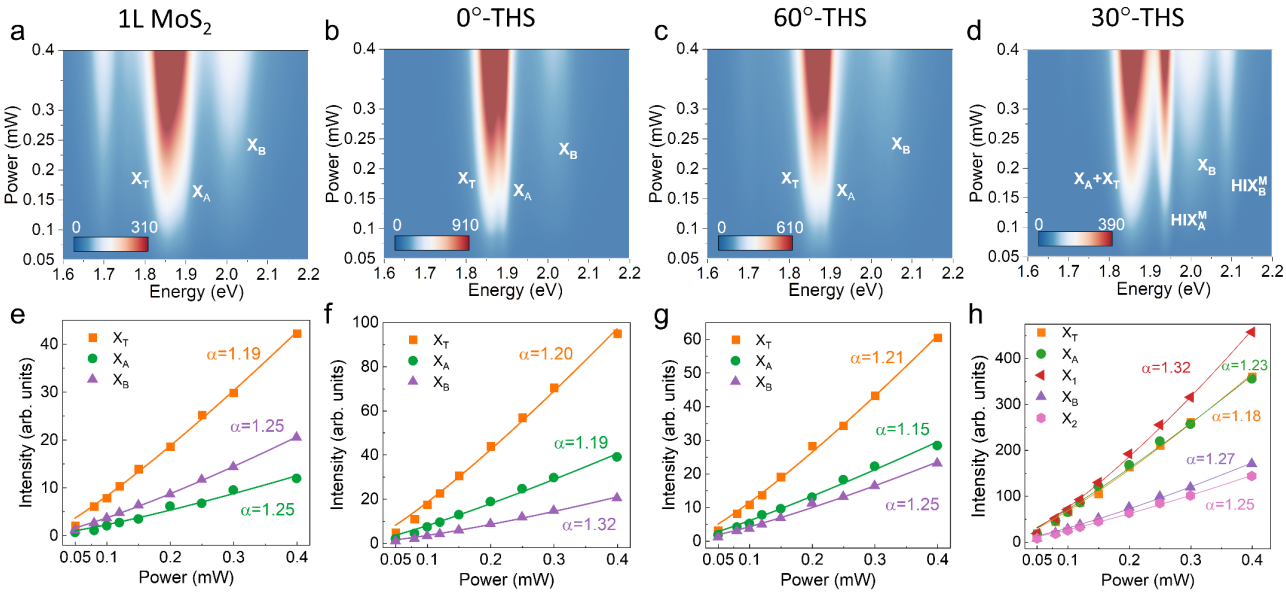

Figure S8. Power-dependent PL spectra. a-d, Color plots of power-dependent PL intensity of 1L MoS_2 (**a**), 0°-THS (**b**), 60°-THS (**c**), and 30°-THS (**d**). **e-h**, PL intensity as a function of power for 1L MoS_2 (**e**), 0°-THS (**f**), 60°-THS (**g**), and 30°-THS (**h**). The solid lines represent the fitting results using $I \propto P^{\alpha}$, where α is the index parameter. X_A, X_T, and X_B exhibit typical free exciton with α≈1. For HIX_A^M and HIX_B^M in moiré quasicrystal, their α values are also near 1 with slightly larger than that corresponding intralayer exciton, indicating the free exciton feature.

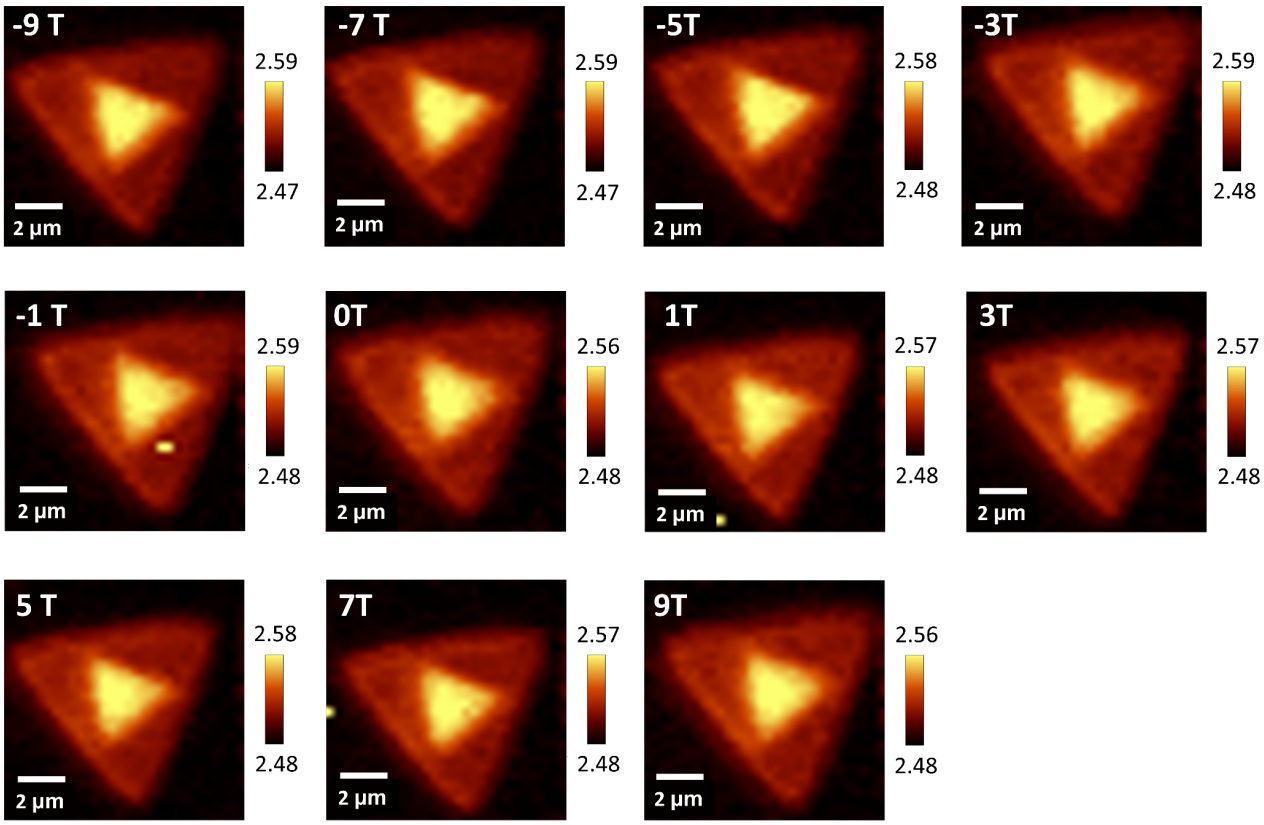

Figure S9. PL mapping in moiré quasicrystal under magnetic field. The magnetic field ranges from -9 to 9 T. Integral PL intensity of HIX_A^M located at 1.941 eV with 49 meV peak width was collected. The zones of 30-THS show strong and averaged PL intensity under any measured magnetic field, indicating the robustness of interlayer exciton in moiré quasicrystal under magnetic field.

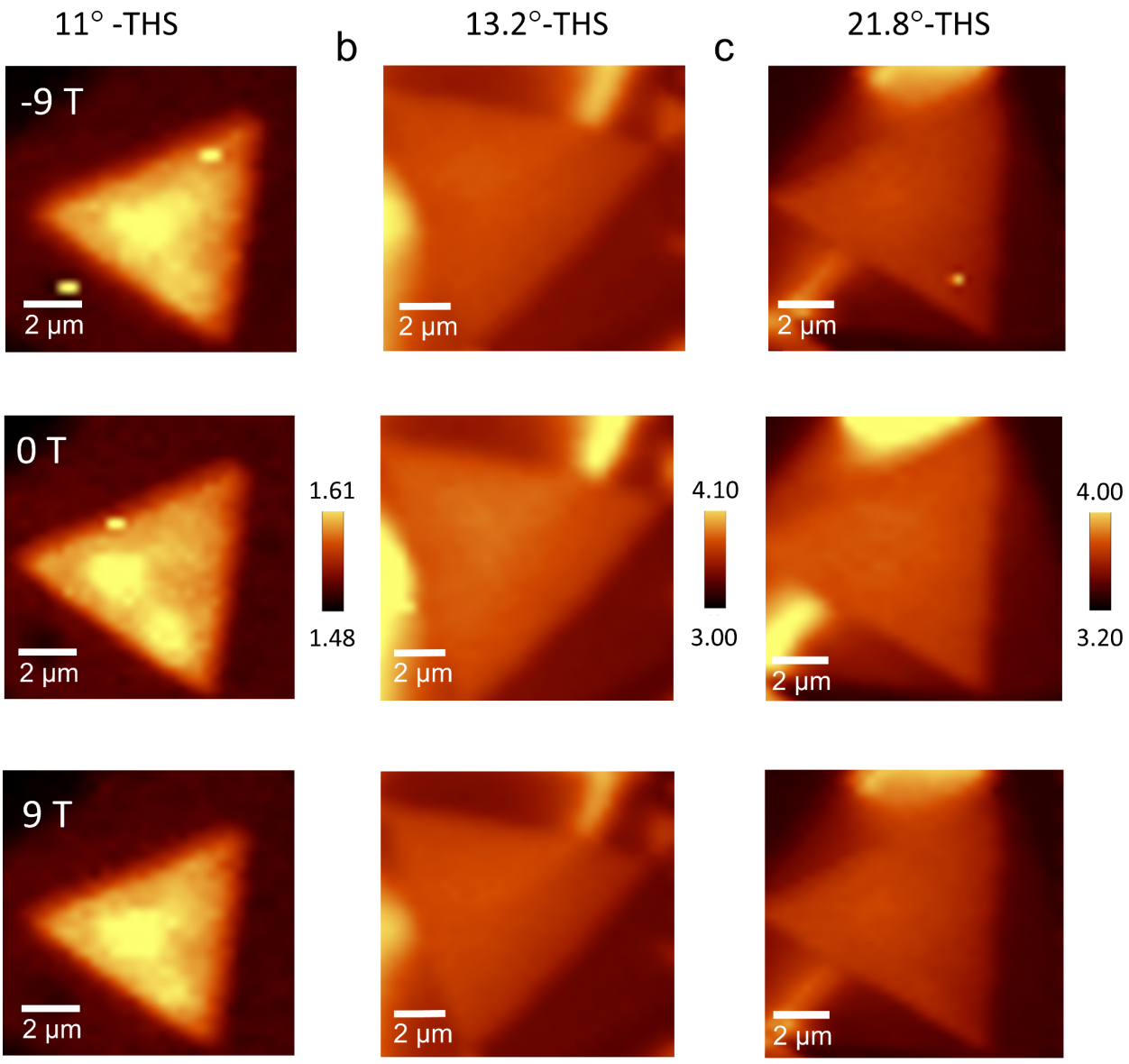

Figure S10. PL mapping of THS with selected twist angle under magnetic field. a-c, PL mapping of 11-THS (a), 13.2-THS (b), and 21.8-THS (c) under -9 (top panels), 0 (medium panels), and 9 T (bottom panels) magnetic field. The magnetic field does not affect the appearance or disappearance of hybridized interlayer exciton.

Supplementary Note 5: Moiré phonon in twisted MoS_2 bilayers

Certain phonon modes in moiré superlattice can be folded into zone center and activated in the Raman spectra by moiré potential and folded effect, giving rise to the folded phonon in the Raman spectra, which is named as moiré phonon.[25] In twisted MoS_2 homobilayers, we observe a moiré

phonon at 416.0-410.4 cm^{-1} in the Raman spectra of MoS_2 bilayers with twist angles ranging from 30° to 11°, which are not observed in 0°-THS and 60°-THS (Figure S11a). These Raman peaks are consistent with the folded A_{1g} (FA_{1g}) modes reported in previous study.[25]

Figure S11b shows the angle-dependent Raman spectra. As the twist angle increases from 0° to 30°, the E^1_{2g} mode first increases and then remains steady, while A_{1g} mode first decreases and then remains steady. As the twisted angles increase from 30° to 60°, the Raman shifts for E^1_{2g} and A1g show a decrease and increase, respectively. For the FA_{1g} mode, the Raman shifts monotonously decrease at the twist angle increases from 11° to 30° (Figure S11b). Furthermore, under a magnetic field, moiré phonon FA_{1g} of moiré quasicrystal still exist as shown in Figure S12.

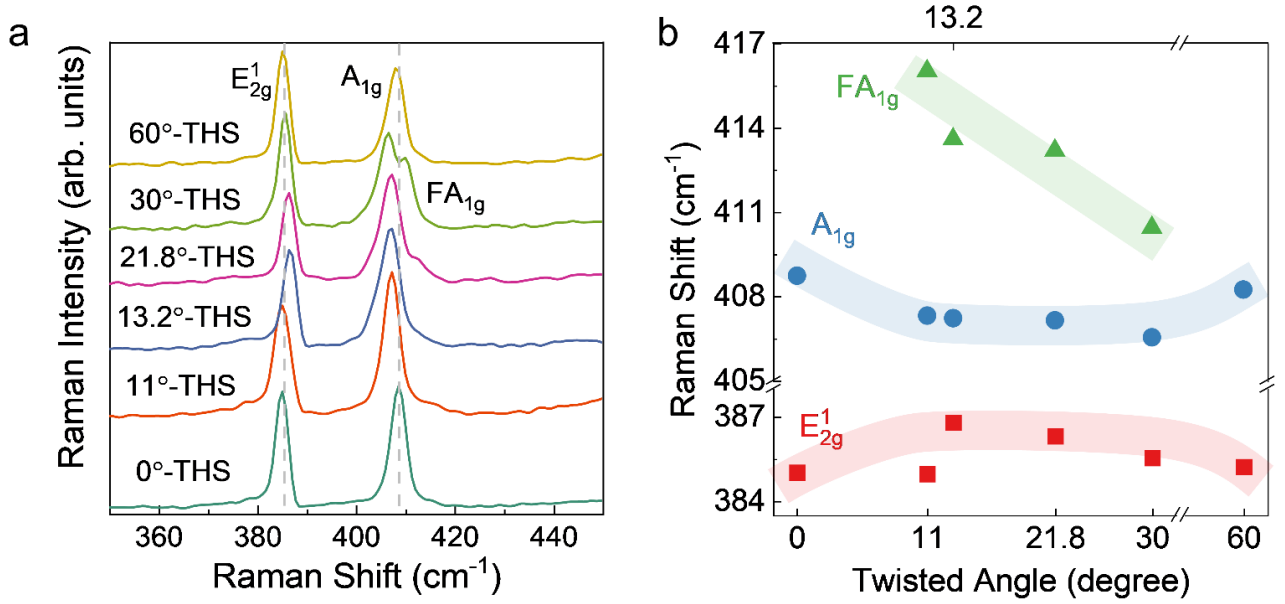

Figure S11. Angle-dependent Raman spectra of twisted MoS_2 bilayers. a, Raman spectra of twisted MoS_2 bilayers at certain twist angle in the wavenumber range of 350-450 cm^{-1}. The Raman peaks located at 411.5 cm^{-1} is the folded A_{1g} (FA_{1g}) mode due to moiré folded effect. **b**, Raman shift as a function of twist angle. As the twist angle increase from 0° to 60°, E^1_{2g} Raman peak experience a process of first increasing, then maintaining stability and then decreasing, in contrary to A_{1g} mode. For FA_{1g} mode, Raman shifts decrease for twist MoS_2 bilayer with the twist angle from 11° to 30°.

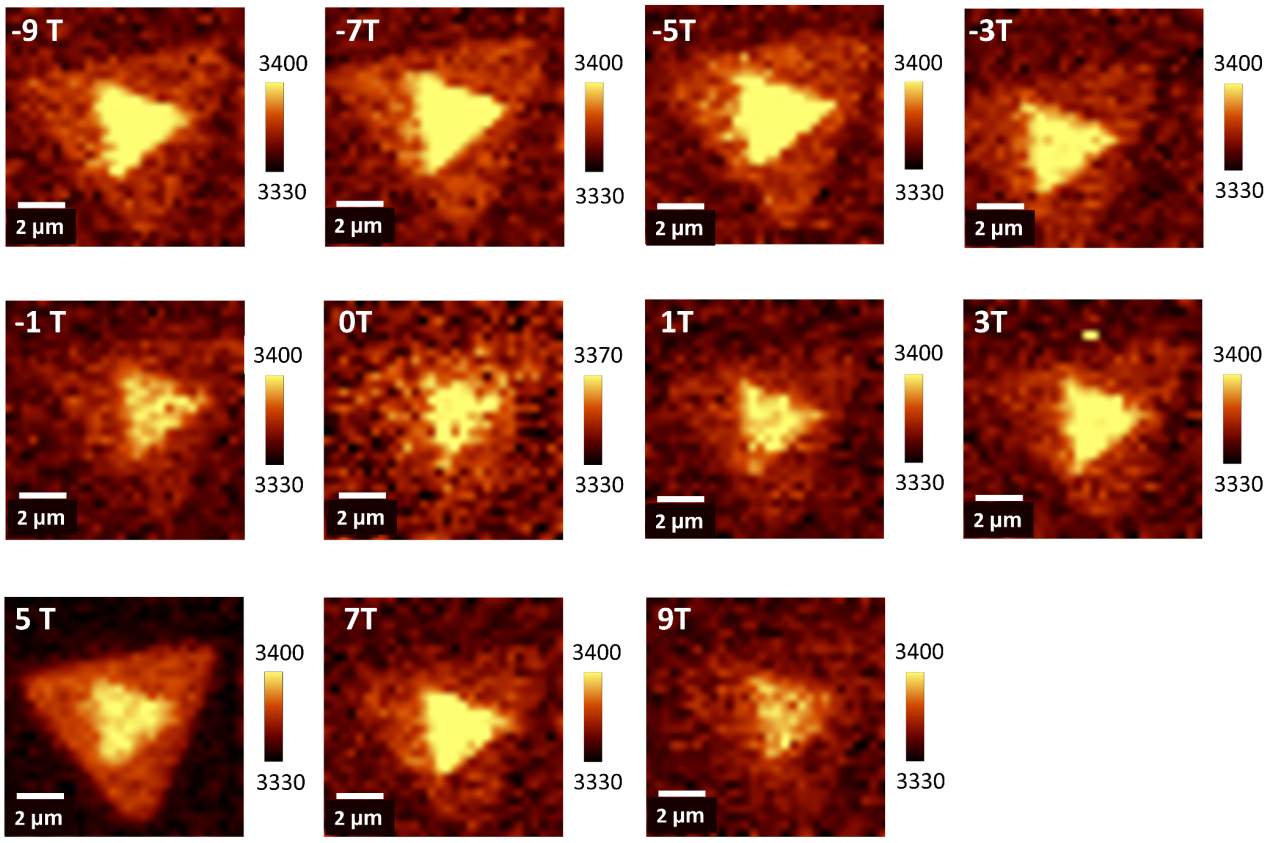

Figure S12. Raman mapping of moiré quasicrystal under magnetic field. The Raman mapping is integral Raman intensity of P1 center wavenumber of 411.5 eV with 4 cm^{-1} peak width. The zones of 30°-THS show strong and averaged Raman intensity under any measured magnetic field.

References

1. Aivazian, G. *et al.* Magnetic control of valley pseudospin in monolayer WSe_2. *Nat. Phys.* **11**, 148-152 (2015).
2. Ciarrocchi, A. *et al.* Polarization switching and electrical control of interlayer excitons in two-dimensional van der Waals heterostructures. *Nat. Photonics* **13**, 131-136 (2018).
3. Lorchat, E. *et al.* Excitons in Bilayer MoS_2 Displaying a Colossal Electric Field Splitting and Tunable Magnetic Response. *Phys. Rev. Lett.* **126**, 037401 (2021).
4. Kormányos, A., Zólyomi, V., Drummond, N. D. & Burkard, G. Spin-Orbit Coupling, Quantum Dots, and Qubits in Monolayer Transition Metal Dichalcogenides. *Phys. Rev. X* **4**, 011034 (2014).
5. Seyler, K. L. *et al.* Signatures of moiré-trapped valley excitons in $MoSe_2/WSe_2$ heterobilayers.

Nature **567**, 66-70 (2019).

6. Li, Z. *et al.* Revealing the biexciton and trion-exciton complexes in BN encapsulated WSe_2. *Nat. Commun.* **9**, 3719 (2018).
7. Chen, S.-Y., Goldstein, T., Taniguchi, T., Watanabe, K. & Yan, J. Coulomb-bound four- and five-particle intervalley states in an atomically-thin semiconductor. *Nat. Commun.* **9**, 3717 (2018).
8. Liu, G. B., Xiao, D., Yao, Y., Xu, X. & Yao, W. Electronic structures and theoretical modelling of two-dimensional group-VIB transition metal dichalcogenides. *Chem. Soc. Rev.* **44**, 2643-2663 (2015).
9. Kormányos, A. *et al.* k·p theory for two-dimensional transition metal dichalcogenide semiconductors. *2D Mater.* **2**, 022001 (2015).
10. Stier, A. V., McCreary, K. M., Jonker, B. T., Kono, J. & Crooker, S. A. Exciton diamagnetic shifts and valley Zeeman effects in monolayer WS_2 and MoS_2 to 65 Tesla. *Nat. Commun.* **7**, 10643 (2016).
11. Mitioglu, A. A. *et al.* Magnetoexcitons in large area CVD-grown monolayer MoS_2 and $MoSe_2$ on sapphire. *Phys. Rev. B* **93**, 165412 (2016).
12. Goryca, M. *et al.* Revealing exciton masses and dielectric properties of monolayer semiconductors with high magnetic fields. *Nat. Commun.* **10**, 4172 (2019).
13. Cadiz, F. *et al.* Excitonic Linewidth Approaching the Homogeneous Limit in MoS_2-Based van der Waals Heterostructures. *Phys. Rev. X* **7**, 021026 (2017).
14. Paradisanos, I. *et al.* Controlling interlayer excitons in MoS_2 layers grown by chemical vapor deposition. *Nat. Commun.* **11**, 2391 (2020).
15. Feng, S. *et al.* Highly tunable ground and excited state excitonic dipoles in multilayer 2H-$MoSe_2$. *Nat. Commun.* **15**, 4377 (2024).
16. Gerber, I. C. *et al.* Interlayer excitons in bilayer MoS_2 with strong oscillator strength up to room temperature. *Phys. Rev. B* **99**, 035443 (2019).
17. Leisgang, N. *et al.* Giant Stark splitting of an exciton in bilayer MoS_2. *Nat. Nanotechnol.* **15**, 901-907 (2020).

18. Sponfeldner, L. *et al.* Capacitively and Inductively Coupled Excitons in Bilayer MoS_2. *Phys. Rev. Lett.* **129** (2022).
19. Slobodeniuk, A. O. *et al.* Fine structure of K-excitons in multilayers of transition metal dichalcogenides. *2D Mater.* **6**, 025026 (2019).
20. Gong, Z. *et al.* Magnetoelectric effects and valley-controlled spin quantum gates in transition metal dichalcogenide bilayers. *Nat. Commun.* **4**, 2053 (2013).
21. Li, Y. *et al.* Tuning commensurability in twisted van der Waals bilayers. *Nature* **625**, 494-499 (2024).
22. Ahn, S. J. *et al.* Dirac electrons in a dodecagonal graphene quasicrystal. *Science* **361**, 782-786 (2018).
23. Liu, Z. *et al.* Field-Tunable Valley Coupling and Localization in a Dodecagonal Semiconductor Quasicrystal. *arXiv preprint arXiv:2408.02176* (2024).
24. O'Donnell, K. P. & Chen, X. Temperature dependence of semiconductor band gaps. *Appl. Phys. Lett.* **58**, 2924-2926 (1991).
25. Lin, M. L. *et al.* Moire Phonons in Twisted Bilayer MoS_2. *ACS Nano* **12**, 8770-8780 (2018).